

12 Multiple-Scattering Formalism for Correlated Systems: a KKR-DMFT Approach

H. Ebert, J. Minár, and D. Ködderitzsch
Department Chemie – Lehrbereich Phys. Chemie
Ludwig-Maximilians-Universität München

Contents

1	Introduction	2
2	The LSDA+DMFT scheme	4
3	Combination of the LSDA+DMFT with the KKR method	6
3.1	General idea of the KKR method	6
3.2	Solution of the single-site problem	7
3.3	Multiple scattering and Green's function	9
3.4	Electronic structure and relativistic extension	11
3.5	The self-consistency cycle	15
3.6	Treatment of disordered alloys	15
4	Applications	17
4.1	Ground state properties	17
4.2	Electron spectroscopy	22
5	Summary	27

1 Introduction

The combination of the DMFT (dynamical mean field theory) with the LSDA (local spin density approximation) led to a very powerful approach to deal with correlations in solid state materials beyond the capability of plain LSDA [1–3]. Due to this attractive feature the LSDA+DMFT has now been implemented on the basis of many different band structure methods during the last years [4]: first in the linear muffin-tin orbital method in the atomic sphere approximation (ASA-LMTO) [5–7] and then in full-potential LMTO [8, 9]. Common to nearly all of these band structure methods is that they are based on the variational principle representing the electronic structure in terms of Bloch functions $\Psi_{j\vec{k}}(\vec{r})$ and eigen energies $E_{j\vec{k}}$. Corresponding LSDA+DMFT calculations are therefore done in several steps: starting from a standard LSDA calculation the corresponding one-electron Green's function $G_{\text{LSDA}}(\vec{k}, E) = [E - H_{\text{LSDA}}(\vec{k})]^{-1}$ is constructed in reciprocal space. In a next step the DMFT self-energy $\Sigma(E)$, that accounts for correlation effects beyond the LSDA level, is included by solving the Dyson equation $G^{-1}(\vec{k}, E) = G_{\text{LSDA}}^{-1}(\vec{k}, E) - \Sigma(E)$. A Brillouin zone integration of $G(\vec{k})$ gives finally the LSDA+DMFT one-electron Green's function $G(E)$ that enters the DMFT-problem. In the next step the DMFT-problem is solved using $G(E)$ as an input and giving a new self-energy $\Sigma(E)$. The last steps are repeated until self-consistency is reached with respect to the one-electron Green's function $G(E)$ and the self-energy Σ (DMFT self-consistency). This sequence of steps is sketched in Fig. 1. In many cases the calculations are stopped here, i.e. after a one-shot

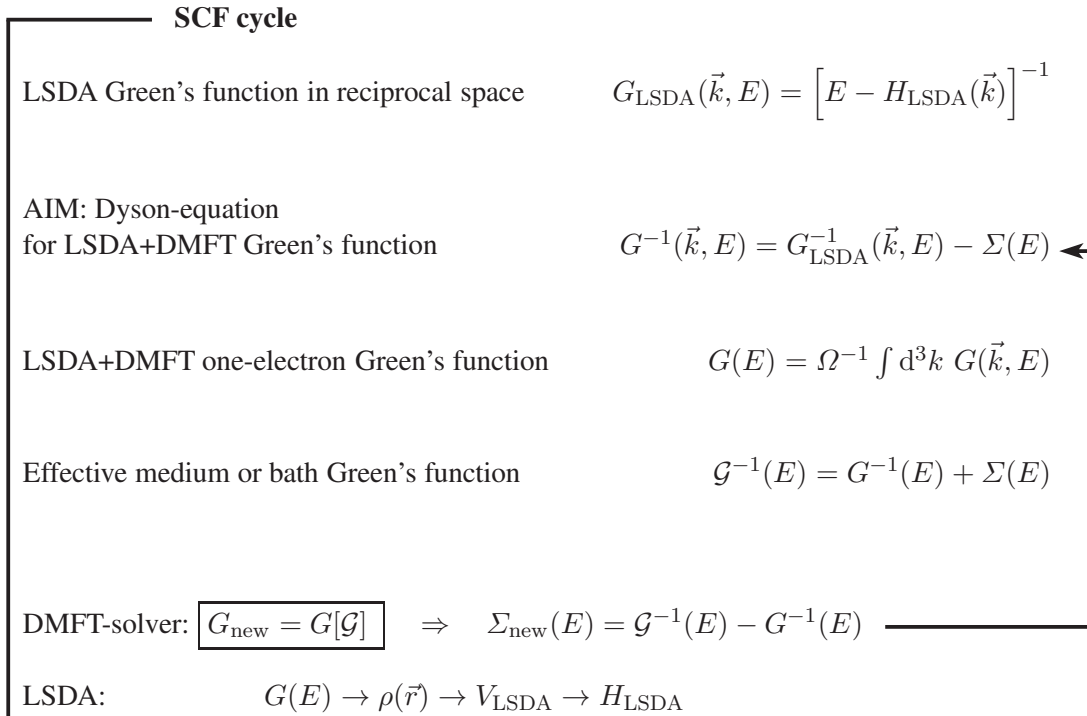


Fig. 1: Scheme for the implementation of the LSDA+DMFT using a standard \vec{k} -space band structure method including the SCF-cycle for the electronic charge $\rho(\vec{r})$ as an outer loop.

inclusion of the DMFT on the basis of a LSDA-calculation. Otherwise the LSDA+DMFT is

performed in a charge self-consistent way by constructing the new charge density from the one-electron Green's function to be used in a standard SCF cycle. To underline the importance of complete LSDA+DMFT self-consistency one should mention that the first successful attempt to combine the DMFT with LSDA charge self-consistency gave an important insight into the long-standing problem of phase diagram and localization in f-electron systems [8, 9] and has been used also to describe correlation effects in half-metallic ferromagnetic materials like NiMnSb [10].

Due to the prominent role of the one-electron Green's function it seems to be highly attractive to implement the LSDA+DMFT scheme using a band structure method that delivers the Green's function directly. This was first done using the LMTO-Green's function method in a non-charge self-consistent way [11]. Subsequently, the so-called EMTO (exact muffin-tin orbital) method was applied in a charge-self-consistent way as a computational framework for the band structure part [12]. In the EMTO approach [13, 14] the one-electron effective potential is represented by the optimized overlapping muffin-tin potential which is considered as the best possible spherical approximation to the full-one electron potential. In essence the one-electron Green's function is evaluated on a complex contour similarly to the screened KKR (Korringa Kohn Rostoker) technique, from which it was derived. In the iteration procedure the LSDA+DMFT Green's function is used to calculate the charge and spin densities. Finally, for the charge self-consistent calculation one constructs the new LSDA effective potential from the spin and charge densities [15], using the Poisson equation in the spherical cell approximation [16]. However, the EMTO-based LSDA+DMFT still follows essentially the scheme sketched above that deals with the DMFT self-energy Σ after having solved the LSDA electronic structure problem. In contrast to this, the KKR implementation [17] follows a natural development in which the self-energy is added directly to the coupled radial differential equations which determine the electronic wave function within a potential well and this way the single-site t -matrix. Because this way also the scattering path operator of multiple scattering theory used to set up the electronic Green's function is determined unambiguously, no further approximations are needed to achieve charge self-consistency.

Representing the electronic structure in terms of the Green's function from the very beginning provides many other advantages: In particular the use of the Dyson equation allows to deal with quite complex systems by connecting the Green's function of a perturbed system with the Green's function of a suitable complementary unperturbed reference system. This gives in particular access to systems without Bloch symmetry [18]. Furthermore, the use of the Coherent Potential Approximation (CPA) alloy theory [19] in combination with Green's function based electronic structure methods allows to deal with substitutional disorder including both diluted impurities and concentrated alloys [20]. The physical condition corresponding to the CPA is simply that a single alloy component embedded in the effective CPA medium should produce no change on the average. A similar philosophy is applied also when dealing with many-body problems for crystals in the framework of the DMFT [21]. Accordingly, the alloy CPA and DMFT can be combined without any conceptual problems [11]. Finally, it should be mentioned

that spectroscopic properties of solids are investigated in a most flexible and powerful way using the Green's function to represent the electronic structure that is probed [22–24]. Thus, an implementation of the LSDA+DMFT using a Green's function based band structure method allows to combine an improved treatment of correlation effects via the DMFT for a wide variety of complex systems with a reliable description of their spectroscopic properties. This is a very attractive feature as it allows on the one-hand side a reliable and detailed interpretation of experimental results and on the other hand to monitor the achievements made by inclusion of correlation effects via the DMFT.

In fact the KKR method of Korringa [25], Kohn and Rostoker [26] is the first band structure method formulated in terms of Green's functions. The obvious advantage of the KKR method lies in the transparent multiple scattering formalism which allows to express the Green's function directly in terms of single-site scattering and geometrical or structural quantities. Thus it seems to be rather natural to combine the DMFT and KKR methods to arrive at a very reliable and flexible band structure scheme that includes correlation effects beyond the standard local density (LSDA) or generalized (GGA) approximations.

2 The LSDA+DMFT scheme

In order to account within LSDA-band structure calculations for correlations an improved hybrid Hamiltonian was proposed by Anisimov et al. [27, 28]. In its most general form such a Hamiltonian is written as

$$H = H_{\text{LSDA}} + H_U - H_{\text{DC}} , \quad (1)$$

where H_{LSDA} stands for the ordinary LSDA Hamiltonian, H_U describes the effective electron-electron interaction and the one-particle Hamiltonian H_{DC} serves to eliminate double counting of the interactions already accounted for by H_{LSDA} .

Using second quantization a rather general expression for H_U is given by:

$$H_U = \frac{1}{2} \sum_{n,ijkl} U_{ijkl}^n \hat{c}_{ni}^\dagger \hat{c}_{nj}^\dagger \hat{c}_{nk} \hat{c}_{nl} , \quad (2)$$

where n runs over all the sites at \vec{R}_n of the crystal and the creation (\hat{c}^\dagger) and annihilation (\hat{c}) operators are defined with respect to some subset of localized orbitals $\phi_i(\vec{r} - \vec{R}_n)$. For the applications presented below these will be the d-orbitals of the transition metals considered. The constants U_{ijkl}^n are matrix elements of the screened Coulomb interaction $v(\vec{r} - \vec{r}')$:

$$U_{ijkl}^n = \int d^3r \int d^3r' \phi_i^\dagger(\vec{r} - \vec{R}_n) \phi_j^\dagger(\vec{r}' - \vec{R}_n) v(\vec{r} - \vec{r}') \phi_k(\vec{r}' - \vec{R}_n) \phi_l(\vec{r} - \vec{R}_n) . \quad (3)$$

The resulting many-particle Hamiltonian can not be diagonalized exactly, thus various methods were developed in the past to find an approximate solution [21]. Among them one of the most promising approaches is to solve Eq. (1) within DMFT that was developed originally to deal with the Hubbard model.

The main idea of the DMFT is to map a periodic many-body problem onto an effective single-impurity problem that has to be solved self-consistently. For this purpose one describes the electronic properties of the system in terms of the one-electron Green's function $\hat{G}(E)$, being the solution of the equation:

$$[E - \hat{H} - \hat{\Sigma}(E)]\hat{G} = \hat{1}, \quad (4)$$

where E is the complex energy and the effective self-energy operator $\hat{\Sigma}(E)$ is assumed to be a single-site quantity for site n :

$$\hat{\Sigma}(E) = \sum_{ij} |\phi_{ni}\rangle \Sigma_{ij}(E) \langle \phi_{nj}|. \quad (5)$$

Fig. 2 shows as an example the spin-dependent self-energy matrix $\Sigma_{ij}(E)$ for ferromagnetic Ni that occurs within Eq. (5). Within DMFT, the self-energy matrix $\Sigma_{ij}(E)$ is a solution of the

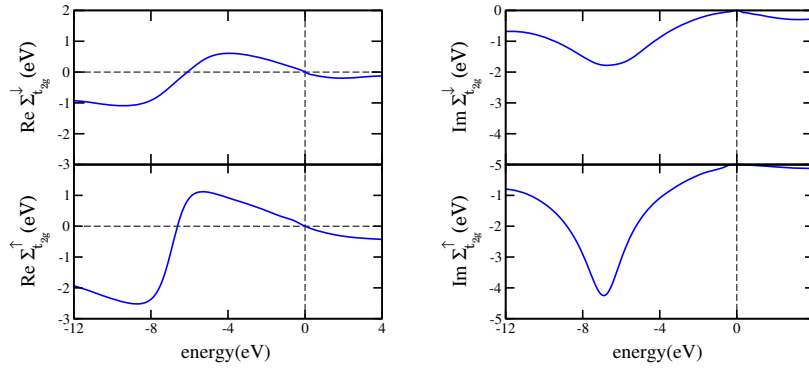


Fig. 2: The spin-dependent self-energy matrix $\Sigma_{ij}(E)$ for ferromagnetic Ni calculated using a DMFT-solver based on the FLEX scheme. Only results for the d -orbitals with t_{2g} -symmetry are shown [17].

many-body problem of an impurity placed in an effective medium. This medium is described by the so called *bath* Green's function matrix \mathcal{G} defined as:

$$\mathcal{G}_{ij}^{-1}(E) = G_{ij}^{-1}(E) + \Sigma_{ij}(E), \quad (6)$$

where the one-electron Green's function matrix $G_{ij}(E)$ is calculated as a projection of $\hat{G}(E)$ onto the impurity site:

$$G_{ij}(E) = \langle \phi_{ni} | \hat{G}(E) | \phi_{nj} \rangle. \quad (7)$$

As the self-energy $\Sigma_{ij}(E)$ depends on the *bath* Green's function $\mathcal{G}_{ij}(E)$ the DMFT equations have to be solved self-consistently. Accordingly, from a technical point of view the problem can be split into two parts. One is dealing with the solution of Eq. (4) and the second one is the effective many-body problem to find the self-energy $\Sigma_{ij}(E)$. The second part can be dealt with in principle by any DMFT-solver as they are presented in the other lectures. To have a reasonable balance between accuracy and computing time within charge self-consistent calculations, one may use for example the perturbative SPTF (spin-polarized T -matrix + FLEX) scheme [29, 30].

3 Combination of the LSDA+DMFT with the KKR method

3.1 General idea of the KKR method

The KKR method in its original version [25, 26] was also a \vec{k} -space band structure method that calculates Bloch wave functions $\Psi_{n\vec{k}}(\vec{r})$ together with the associated eigen energies $E_{n\vec{k}}$ by solving the Lippmann-Schwinger equation complementary to the Schrödinger equation for a periodic potential $V(\vec{r})$. The free electron gas was used as the reference system with its corresponding one-electron Green's function $G^0(\vec{r}, \vec{r}', E)$ in real space. This scheme was later extended by various authors [31] to determine the one-electron Green's function $G(\vec{r}, \vec{r}', E)$ of a solid on the basis of the Dyson equation that again uses the free electron gas as the reference system. Obviously, this scheme can be used without major modifications for an implementation of the LSDA+DMFT leading to the following Dyson equation:

$$G(\vec{r}, \vec{r}', E) = G^0(\vec{r}, \vec{r}', E) + \int d^3r'' \int d^3r''' G^0(\vec{r}, \vec{r}'', E) \left[V_{\text{LSDA}}(\vec{r}'')\delta(\vec{r}'' - \vec{r}''') + \Sigma(\vec{r}'', \vec{r}''', E) \right] G(\vec{r}''', \vec{r}', E). \quad (8)$$

Here $V_{\text{LSDA}}(\vec{r})$ is the local, real and energy-independent LSDA-based potential while the self-energy $\Sigma(\vec{r}, \vec{r}', E)$ is non-local, complex and energy-dependent. In the following it is assumed that the self-energy is site-diagonal, i.e. $\Sigma(\vec{r}, \vec{r}', E)$ is non-zero only if \vec{r} and \vec{r}' are within the same atomic cell n . This is well justified in most cases and allows to use the standard KKR approach to deal with Eq. (8). It should be mentioned, however, that taking $\Sigma(\vec{r}, \vec{r}', E)$ to be site-diagonal is not a necessary requirement for a KKR-based implementation. This implies in particular that extensions necessary to deal with a cluster formulation of the DMFT or a \vec{k} -dependent self-energy are possible.

Within the KKR method the Dyson equation (8) is solved by application of multiple scattering theory. This formalism splits the problem into two parts. In a first step the LSDA- or here the LSDA+DMFT-based Schrödinger-like equation is solved for each inequivalent atomic site n in the system (single-site problem). This implies that for a given energy E the corresponding wave functions $\Psi(\vec{r}, E)$ are calculated that in turn can be used to set up the single-site t -matrix $t_{LL'}^n(E)$ in an angular momentum representation ($L = (l, m_l)$). In a second step, the multiple scattering problem for the solid is solved assuming free-electron like propagation of the electrons between the atomic sites n . The corresponding Green's function of the free electron gas is represented by the so-called structure constants $G_{LL'}^{0nn'}(E)$ that contain only structural information on the system. For periodic solids the multiple scattering problem is solved by a Fourier transformation and $G_{LL'}^0(\vec{k}, E)$ depends on the wave vector \vec{k} accordingly. For finite systems, the multiple scattering problem can also be solved directly in real space [18]. Within the KKR-formalism, the solution of the multiple scattering problem is represented by the so-called scattering path operator $\tau_{LL'}^{nn'}(E)$ that describes the transfer of an electronic wave with character L' at site n'

to a wave with character L at the site n with all possible scattering events in between self-consistently taken into account. With the scattering path operator $\tau_{LL'}^{nn'}(E)$ available the Green's function $G(\vec{r}, \vec{r}', E)$ of the system can be set up straight forwardly. The sequence of the various steps of a KKR-implementation are shown in Fig. 3.

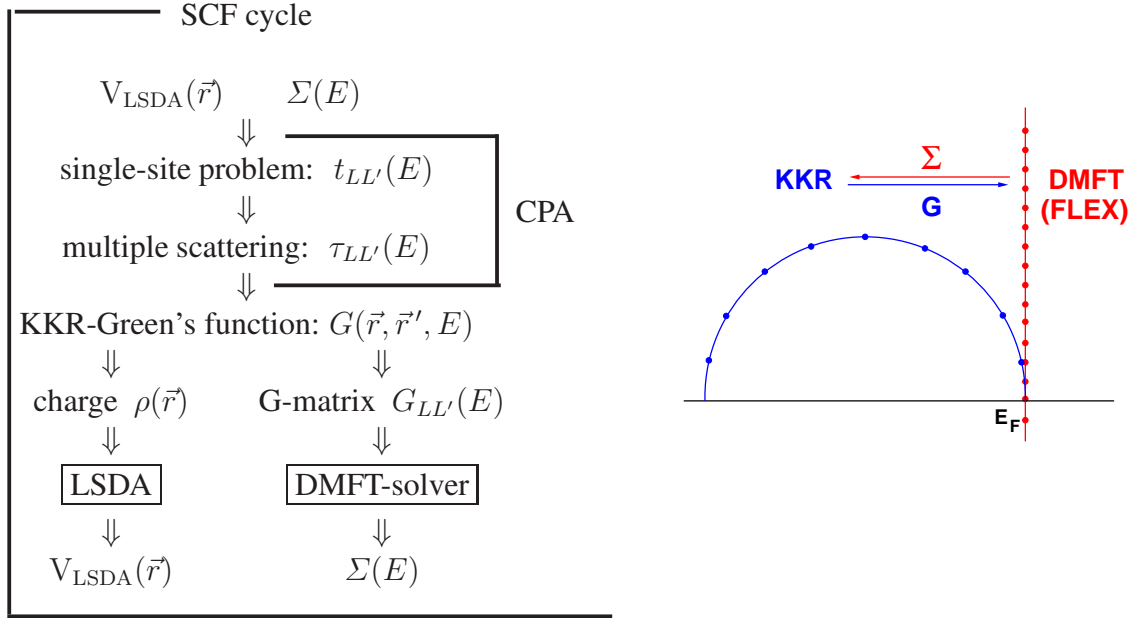


Fig. 3: LSDA+DMFT scheme as implemented on the basis of the KKR formalism. The right part of the figure shows the various energy contours used in case of using a FLEX DMFT-solver (see text).

This brief description of the KKR-formalism makes clear that going from the LSDA to the LSDA+DMFT affects only the single-site but not the multiple scattering problem. This also implies that the DMFT self-energy Σ already enters the scheme when calculating the basis functions. As can be seen from the Dyson equation (8) the LSDA- and DMFT-parts of the electronic structure problem of the solid are accordingly dealt with on the same level.

3.2 Solution of the single-site problem

The solution of the single-site problem including the DMFT self-energy can be worked out following the full-potential description of the KKR formalism [32]. In terms of the wave functions the single-site quasi particle equation to be solved for each spin channel σ reads

$$[-\vec{\nabla}^2 + V^\sigma(r) - E]\Psi(\vec{r}, E) + \int \Sigma^\sigma(\vec{r}, \vec{r}', E) \Psi(\vec{r}', E) d^3r' = 0. \quad (9)$$

In the following the spin index σ is omitted for the moment keeping in mind that for a spin-polarized system described in a non-relativistic way, one has to solve Eq. (9) for each spin channel (see for example Fig. 2) independently. For a particular solution $\Psi_\nu(\vec{r}, E)$ labeled by

the index ν one can start from the ansatz:

$$\Psi_\nu(\vec{r}, E) = \sum_L \Psi_{L\nu}(\vec{r}, E), \quad (10)$$

where the partial waves $\Psi_{L\nu}(\vec{r}, E)$ are chosen to have the same form as the linearly independent solutions for the spherically symmetric potential:

$$\Psi_{L\nu}(\vec{r}, E) = \Psi_{L\nu}(r, E)Y_L(\hat{r}), \quad (11)$$

with $L = (l, m_l)$ standing for the angular momentum and magnetic quantum numbers and $Y_L(\hat{r})$ are spherical harmonics. Inserting the ansatz (10) into the single-site equation (9) and integrating over angle variables leads to the following set of the coupled radial integro-differential equations:

$$\left[\frac{d^2}{dr^2} - \frac{l(l+1)}{r^2} - V(r) + E \right] \Psi_{L\nu}(r, E) = \int d^3r' \Sigma(\vec{r}, \vec{r}', E) \Psi_{L\nu}(\vec{r}', E), \quad (12)$$

where the basis functions $\phi_L(\vec{r}) = \phi_l(r)Y_L(\hat{r})$ will be normalized and suitably chosen d-like wave functions when dealing with transition metals.

For a general non-diagonal self-energy a radial equation similar to Eq. (12) has to be solved to get the so-called left-hand solutions. This implies one has to consider the two adjoint equations [33]:

$$(\hat{H} + \hat{\Sigma} - E)|\Psi\rangle = 0 \quad (13)$$

$$\langle\Psi^\times|(\hat{H} + \hat{\Sigma} - E) = 0, \quad (14)$$

where the superscript \times is used to distinguish the left hand solution $|\Psi^\times\rangle$ from the standard right hand solution $|\Psi\rangle$.

In principle these equations can be solved by summing a corresponding Born series. So far, however, the equations have been simplified taking advantage of the following special representation for the self-energy:

$$\begin{aligned} \int d^3r' \Sigma(\vec{r}, \vec{r}', E) \Psi_{L\nu}(\vec{r}', E) &= \sum_L \int d^3r' \Sigma_{L'L}(E) \phi_{L'}^\dagger(\vec{r}) \phi_L(\vec{r}') \Psi_{L\nu}(\vec{r}', E) \\ &\approx \sum_L \Sigma_{L'L}(E) \Psi_{L\nu}(\vec{r}, E). \end{aligned} \quad (15)$$

This way the integro-differential equation Eq. (12) becomes a pure differential equation:

$$\left[\frac{d^2}{dr^2} - \frac{l(l+1)}{r^2} - V(r) + E \right] \Psi_{L\nu}(r, E) = \sum_{L'} \Sigma_{LL'}(E) \Psi_{L'\nu}(r, E). \quad (16)$$

After having solved the set of coupled equations for the wave functions one gets the corresponding single-site t -matrix by introducing the auxiliary matrices a and b [20]:

$$\begin{aligned} a_{L\nu}(E) &= -ipr^2 [h_L^-(pr), \Psi_L'(r)]_r \\ b_{L\nu}(E) &= -ipr^2 [h_L^+(pr), \Psi_L'(r)]_r. \end{aligned} \quad (17)$$

Here $p = \sqrt{E}$ is the momentum, $h_L^\pm(pr)$ are Hankel functions of the first and second kind and $[\dots]_r$ denotes the Wronskian. Evaluating the Wronskians at Wigner-Seitz radii r_{WS} that defines the range of the potential associated with site n one finally has (in matrix notation) [20, 34]:

$$\underline{t}(E) = \frac{i}{2p} [\underline{a}(E) - \underline{b}(E)] \underline{b}^{-1}(E) . \quad (18)$$

The regular wave functions Z used to set up the electronic Green's function within the KKR-formalism [35] are obtained by a superposition of the wave functions Ψ_ν according to the boundary conditions at $r = r_{\text{WS}}$:

$$Z_L(\vec{r}, E) = \sum_\nu C_L^\nu \Psi_\nu(\vec{r}) \xrightarrow{r=r_{\text{WS}}} \sum_{L'} j_{L'}(\vec{r}, E) t(E)_{L'L}^{-1} - ip h_L^+(\vec{r}, E) . \quad (19)$$

The irregular solutions J_L needed in addition are fixed by the boundary condition

$$J_L(\vec{r}, E) \xrightarrow{r=r_{\text{WS}}} j_L(\vec{r}, E) \quad (20)$$

with the functions j_L being the spherical Bessel functions.

3.3 Multiple scattering and Green's function

Instead of considering the single-site problem for the wave function $\psi_n(\vec{r}, E)$ in terms of the Lippmann-Schwinger equation (9) one can alternatively deal with the single-site Green's function $G^n(\vec{r}, \vec{r}', E)$ in terms of the corresponding Dyson equation with the potential and self-energy restricted to site n (see Eq. (8)). Ignoring the self-energy Σ for the moment and representing all quantities by their associated operators this may be written as [36]:

$$\hat{G}^n(E) = \hat{G}^0(E) + \hat{G}^0(E) \hat{V}^n \hat{G}^n(E) . \quad (21)$$

The single-site t -matrix $t_i^n(E)$ used above to account for the matching of the wave functions $\Psi_{L\nu}^n(r, E)$ at the radius $r = r_{\text{WS}}$ is related to a corresponding single-site t -matrix operator $\hat{t}^n(E)$ that allows to write an explicit expression for $\hat{G}^n(E)$ [36]:

$$\hat{G}^n(E) = \hat{G}^0(E) + \hat{G}^0(E) \hat{t}^n(E) \hat{G}^0(E) . \quad (22)$$

Completely analogous equations emerge when one is dealing with an array of scatterers [36]:

$$\hat{G} = \hat{G}^0(E) + \hat{G}^0(E) \hat{V} \hat{G}(E) \quad (23)$$

$$= \hat{G}^0(E) + \hat{G}^0(E) \hat{T}(E) \hat{G}^0(E) , \quad (24)$$

where all quantities refer now to the total system. Decomposing all scattering processes into sequences of single-site scattering events, represented by single-site t -matrix operators $\hat{t}^n(E)$, and free propagation according to $\hat{G}^0(E)$ in-between, one may decompose the total t -matrix operator $\hat{T}(E)$ accordingly. This central idea of multiple scattering theory is illustrated by Fig. 4. Using the scattering path operator $\hat{\tau}^{nn'}(E)$ introduced by Gyorffy and Stott [37] one

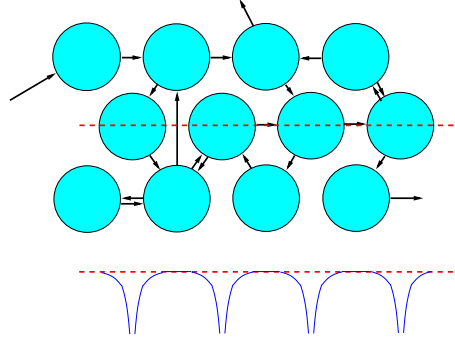


Fig. 4: Central idea of multiple scattering theory: decomposition of electronic motion into scattering at atomic sites and free-electron like propagation in between. The bottom of the figure gives a sketch for the potential along the dashed line.

gets [36, 38]:

$$\hat{T}(E) = \sum_{nn'} \hat{\tau}^{nn'}(E), \quad (25)$$

where $\hat{\tau}^{nn'}(E)$ is defined to transfer an electronic wave incoming at site n' into a wave outgoing from site n with all possible scattering events that may take place in-between in a self-consistent way. Adopting an angular momentum representation as introduced in the previous section, this requirement implies for the corresponding matrix the following equation of motion

$$\underline{\tau}^{nn'}(E) = \underline{t}^n(E) \delta_{nn'} + \underline{t}^n(E) \sum_{k \neq n} \underline{G}^{0nk}(E) \underline{\tau}^{kn'}(E), \quad (26)$$

where the underline indicates matrices with respect to L with $(\underline{\tau}^{nn'})_{LL'} = \tau_{LL'}^{nn'}$ etc. For a finite system this equation is solved straight forwardly by a matrix inversion [39]:

$$\underline{\underline{\tau}}(E) = [\underline{\underline{t}}(E)^{-1} - \underline{\underline{G}}^0(E)]^{-1}, \quad (27)$$

where $\underline{\underline{M}} = [\underline{\underline{t}}^{-1} - \underline{\underline{G}}^0]$ is the so-called real-space KKR-matrix. The double underline indicates matrices with respect to the angular momentum and site indices, L and n , respectively, with $[\underline{\underline{\tau}}]_{nn'} = \underline{\tau}^{nn'}$, $[\underline{\underline{G}}^0]_{nn'} = \underline{G}^{0nn'}$ and $[\underline{\underline{t}}]_{nn'} = \underline{t}^n \delta_{nn'}$. The energy argument has been dropped here. Dealing with a three-dimensional periodic system Eq. (26) can also be solved exactly by Fourier transformation leading to [36, 38]:

$$\underline{\tau}^{nn'}(E) = \frac{1}{\Omega_{\text{BZ}}} \int_{\Omega_{\text{BZ}}} d^3k [\underline{t}(E)^{-1} - \underline{G}^0(\vec{k}, E)]^{-1} e^{i\vec{k} \cdot (\vec{R}_n - \vec{R}_{n'})}, \quad (28)$$

with the (reciprocal space) structure constants matrix $\underline{G}^0(\vec{k}, E)$ being the Fourier transformed of the real-space structure constants matrix $\underline{\underline{G}}^0(E)$ that represent the free-electron like propagation.

Having constructed a set of regular (Z) and irregular (J) solutions of the single-site problem together with the t -matrix and solved the multiple-scattering problem in Eq. (26) subsequently,

the corresponding Green's function is obtained from the expression [35]:

$$G(\vec{r}_n + \vec{R}_n, \vec{r}'_m + \vec{R}_m, E) = \sum_{LL'} Z_L(\vec{r}_n, E) \tau_{LL'}^{nm}(E) Z_{L'}^\times(\vec{r}'_m, E) - \delta_{nm} \sum_L [Z_L(\vec{r}_n, E) J_L^\times(\vec{r}'_n, E) \Theta(r'_n - r_n) + J_L(\vec{r}_n, E) Z_L^\times(\vec{r}'_n, E) \Theta(r_n - r'_n)]. \quad (29)$$

Given the local nature of the many-body solver used within the DMFT approach, the KKR Green's function in Eq. (29) has to be projected accordingly to the matrix $G_{LL'}^{nm}$ (see Eq. (7)). The projection is performed through the following integration:

$$G_{LL'}^{nm}(E) = \sum_{L_1 L_2} \left(\int d^3 r \phi_L^\dagger(\vec{r}) Z_{L_1}(\vec{r}, E) \right) \tau_{L_1 L_2}^{nm}(E) \left(\int d^3 r' Z_{L_2}^\times(\vec{r}', E) \phi_{L'}(\vec{r}') \right) - \delta_{nm} \sum_{L_1} \left[\int d^3 r' \left(\int_0^{r'} d^3 r \phi_L^\dagger(\vec{r}) Z_{L_1}(\vec{r}, E) \right) J_{L_1}^\times(\vec{r}', E) \phi_{L'}(\vec{r}') + \int d^3 r' \left(\int_{r'}^{r_{\text{WS}}} d^3 r \phi_L^\dagger(\vec{r}) J_{L_1}(\vec{r}, E) \right) Z_{L_1}^\times(\vec{r}', E) \phi_{L'}(\vec{r}') \right]. \quad (30)$$

The Green's function matrix $G_{LL'}^{nm}(E)$ (actually $G_{LL'}^{\sigma nm}(E)$ for both spin channels) represents the input into the solution of the effective impurity problem. As the DMFT-approach concentrates on the correlation among electrons of the same angular momentum l only the $l-l$ -subblock of this matrix will be used in the following. For the transition metal systems dealt here this implies that only the d-d-subblock is considered with $\phi_L(\vec{r})$ being appropriate reference wave functions with $l = 2$.

3.4 Electronic structure and relativistic extension

With the Green's function available the most prominent electronic properties of a solid may be expressed and calculated in a straight forward way. For example the density of states (DOS) $n(E)$, the electron density $\rho(\vec{r})$ and the expectation value of a one-electron operator \mathcal{A} may be obtained from the expressions

$$n(E) = -\frac{1}{\pi} \Im \int_V d^3 r G^+(\vec{r}, \vec{r}, E) \quad (31)$$

$$\rho(\vec{r}) = -\frac{1}{\pi} \Im \int^{E_F} dE G^+(\vec{r}, \vec{r}, E) \quad (32)$$

$$\langle \mathcal{A} \rangle = -\frac{1}{\pi} \Im \int^{E_F} dE \int_V d^3 r \mathcal{A} G^+(\vec{r}, \vec{r}, E), \quad (33)$$

where V is the volume associated with the atom at site n . As an example Fig. 5 shows the spin-resolved density of states $n^{\uparrow(\downarrow)}(E)$ calculated for fcc-Ni on the basis of the LSDA and LSDA+DMFT. Obviously, one can note three prominent changes in the DOS when going

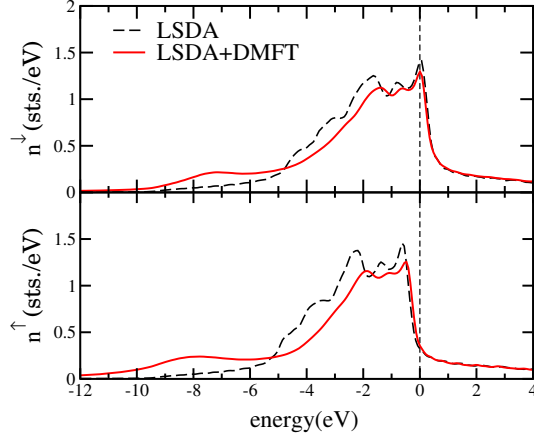


Fig. 5: Spin-resolved density of states $n^{\uparrow(\downarrow)}(E)$ for fcc-Ni calculated via the LSDA and LSDA+DMFT. The upper (lower) panel shows the DOS for the minority (majority) spin [17].

from the LSDA to the LSDA+DMFT: The DOS curves show much less structures and appear smeared-out, the band width shrinks and a satellite peak at around 7 - 8 eV binding energy occurs. All these features can be traced back to the characteristics of the self-energy Σ shown in Fig. 2. In particular one can ascribe the smearing out of the DOS to the imaginary part of Σ while the shrinking of the band width and the satellite is associated with its real part.

To allow for a more detailed discussion of the electronic structure one may introduce the Bloch spectral function $A_B(\vec{k}, E)$ by a Fourier transformation of the real space Green's function $G(\vec{r}, \vec{r}', E)$

$$A_B(\vec{k}, E) = -\frac{1}{\pi N} \sum_{n,m} e^{i\vec{k}(\vec{R}_n - \vec{R}_m)} \Im \int_{\Omega} d^3r \left\langle G(\vec{r} + \vec{R}_n, \vec{r} + \vec{R}_m, E) \right\rangle. \quad (34)$$

For an ordered system dealt with on the basis of the LSDA this leads simply to a set of δ -functions representing the conventional dispersion relation $E_{j\vec{k}}$. Calculating $A_B(\vec{k}, E)$, however, on the basis of the LSDA+DMFT the imaginary part of the self-energy leads to a corresponding broadening, that reflects the finite life time of electronic states with fixed \vec{k} -vector. Corresponding results are shown in Fig. 6 for fcc-Ni. As one notes, the shrinking of the band width and the broadening of the bands take place primarily in the d-band regime.

For the sake of clarity the KKR formulation has been introduced above on a non-relativistic level. For many situations, however, relativistic corrections to the Schrödinger equation play a central role. In fact the interplay of relativistic effects and correlations have been investigated already by various authors on the basis of the LSDA+DMFT [41, 8, 42, 29, 43–45]. Obviously, the most reliable treatment is achieved on the basis of the fully relativistic Dirac formalism. Ignoring the self-energy for the moment this takes the form [46]:

$$\left[\frac{\hbar}{i} c \vec{\alpha} \cdot \vec{\nabla} + \beta m c^2 + \bar{V}(\vec{r}) + \underbrace{\beta \vec{\sigma} \cdot \vec{B}_{\text{eff}}(\vec{r})}_{V_{\text{spin}}(\vec{r})} \right] \Psi(\vec{r}, E) = E \Psi(\vec{r}, E), \quad (35)$$

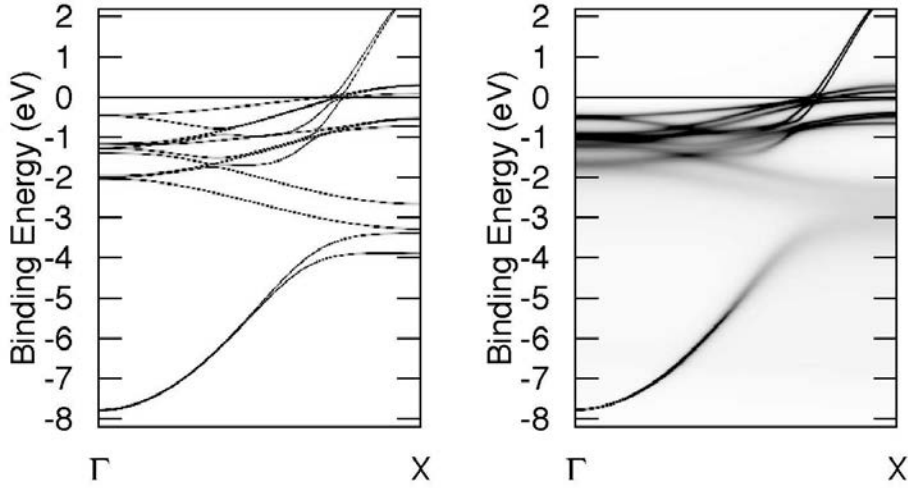


Fig. 6: Band structure of ferromagnetic Ni for \vec{k} along $\overline{\Gamma X}$. Left: LSDA-based dispersion relation $E_{j\vec{k}}$, right: LSDA+DMFT-based Bloch spectral function $A_B(\vec{k}, E)$ [40].

where α_i and β are the standard 4×4 Dirac matrices [47] and $\bar{V}(\vec{r})$ is the scalar Coulomb and spin-averaged part of the exchange-correlation potential. The spin-dependent part $V_{\text{spin}}(\vec{r})$ of the latter one is represented by an effective magnetic field

$$\vec{B}_{\text{eff}}(\vec{r}) = \frac{\delta E_{\text{xc}}[n, \vec{m}]}{\delta \vec{m}(\vec{r})} \quad (36)$$

that is determined by the spin magnetization $\vec{m}(\vec{r})$. Assuming a collinear spin magnetization within an atomic cell one can always choose \hat{z}' such to have:

$$V_{\text{spin}}(\vec{r}) = \beta \sigma_{z'} B_{\text{eff}}(r). \quad (37)$$

To deal with the KKR single-site problem the ansatz

$$\Psi_{\nu}(\vec{r}, E) = \sum_{\Lambda} \Psi_{\Lambda\nu}(\vec{r}, E) = \sum_{\Lambda} \begin{pmatrix} g_{\Lambda\nu}(r, E) \chi_{\Lambda}(\hat{r}) \\ i f_{\Lambda\nu}(r, E) \chi_{-\Lambda}(\hat{r}) \end{pmatrix} \quad (38)$$

is made for the four-component wave function $\Psi_{\nu}(\vec{r}, E)$ in analogy to Eq. (10). Here the partial waves $\Psi_{\Lambda\nu}(\vec{r}, E)$ are constructed using the radial functions, $g_{\Lambda\nu}(r, E)$ and $f_{\Lambda\nu}(r, E)$, of the large and small, respectively, components together with the spin-angular functions [47]

$$\chi_{\Lambda}(\hat{r}) = \sum_{m_s = \pm 1/2} C(l\frac{1}{2}j; \mu - m_s, m_s) Y_l^{\mu - m_s}(\hat{r}) \chi_{m_s} \quad (39)$$

with the Clebsch-Gordon coefficients $C(l\frac{1}{2}j; \mu - m_s, m_s)$ and the short hand notation $\Lambda = (\kappa, \mu)$ and $-\Lambda = (-\kappa, \mu)$ for the relativistic spin-orbit and magnetic quantum numbers, κ and μ , respectively. Obviously, the spin-angular functions $\chi_{\Lambda}(\hat{r})$ are the relativistic counter part to the spherical harmonics occurring in Eq. (10). In particular they are eigen functions to the square of the total angular momentum operator \vec{j}^2 , its z-component j_z as well as the spin-orbit operator

\hat{K} with the eigen values $j(j+1)$, μ and $-\kappa$, respectively, with the quantum numbers restricted by the relations $j = l \pm \frac{1}{2}$, $\mu = -j \cdots + j$, $\kappa = l = j + \frac{1}{2}$ for $j = l - \frac{1}{2}$ and $\kappa = -l - 1 = -j - \frac{1}{2}$ for $j = l + \frac{1}{2}$ [47].

Inserting the ansatz in Eq. (38) into the Dirac equation (35) leads to a coupled set of radial equations for the radial functions $g_{\Lambda\nu}(r, E)$ and $f_{\Lambda\nu}(r, E)$ in analogy to Eq. (16). With an extension of Eqs. (16) through (18) the corresponding single-site t -matrix can finally be evaluated [48]. This scheme implies that the spin-polarization i.e. magnetization of a solid is treated on the same footing as all relativistic effects – in particular the spin-orbit coupling. Complementing the LSDA potential $V(\vec{r})$ with the DMFT self-energy Σ , as done in Eq. (12) leads to a coherent treatment of all relativistic and correlation effects as well as spin-polarization when solving the single-site problem. Treatment of the multiple-scattering problem is done again in full analogy to the non-relativistic formalism described by Eqs. (21) through (28).

The relativistic approach sketched above was formulated in the (κ, μ) -representation. Restricting the expansion of the wave functions $\Psi_{\Lambda\nu}$ in Eq. (38) up to the angular momentum $l_{\max} = 2$ the resulting matrices have the dimension $2(l_{\max} + 1)^2 = 18$. Accounting for correlation effects by means of the DMFT scheme for transition metals implies that the corresponding one-electron Green's function matrix $G_{\Lambda\Lambda'}$ for the d-electrons has the dimension 10. To deal with the DMFT the (l, m_l, m_s) -representation is more suitable implying that one has spin-flip components like $G_{m_l m'_l}^{\uparrow\downarrow}$ for the Green's function matrix because of the inclusion of spin-orbit coupling. As a consequence the DMFT self-energy Σ will also be a 10×10 matrix with spin-flip components. As an example Fig. 12 shows corresponding results for the d-states of Ni in fcc-Ni and for the f-states of U in ferromagnetic US. As one can see, the spin-flip components $\Sigma^{\downarrow\uparrow}$ are quite small

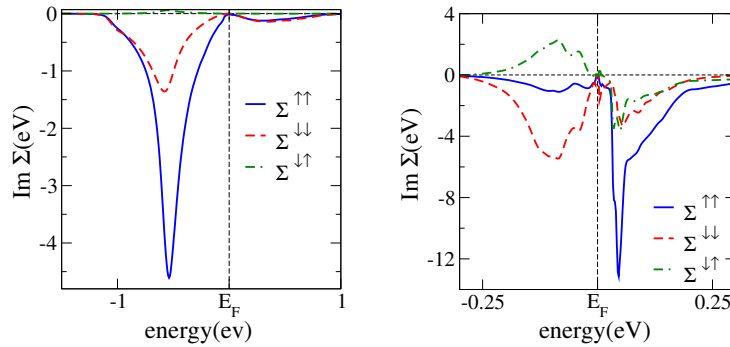


Fig. 7: Spin-dependent self-energy $\Sigma^{m_s m'_s}(E)$ of the d-states of Ni in fcc-Ni (left) and the f-states of U in ferromagnetic US (right) (unpublished).

compared to the spin-diagonal ones $\Sigma^{m_s m_s}$ in the case of Ni. For U on the other hand, they are much larger and comparable to $\Sigma^{m_s m_s}$. This is explained of course by the high atomic number of U and the strong spin-orbit coupling associated with this.

3.5 The self-consistency cycle

A flow chart depicting the self-consistent LSDA+DMFT approach is shown in Fig. 3. The radial equations Eq. (12) provide the set of regular (Z) and (J) irregular solutions of the single-site problem. Together with the t -matrix, the scattering path operator τ and the KKR Green's function is constructed via Eq. (29). To solve the many-body problem the projected impurity Green's function matrix is constructed according to Eq. (30). The LSDA Green's function $G_{LL'}^{nn}(E)$ is calculated on a complex contour (semi circle) which encloses the valence band one-electron energy poles. The Padé analytical continuation is used to map the complex local Green's function $G_{LL'}^{nn}(E)$ on the Matsubara axis which is used when dealing with the many-body problem. For most applications the perturbative SPTF (spin-polarized T -matrix + FLEX) solver of the DMFT problem has been used so far. In fact any DMFT solver could be included which supplies the self-energy $\Sigma(E)$ as a solution of the many-body problem. The Padé analytical continuation is used once more to map back the self-energy from the Matsubara axis to the complex plane, where the new local Green's function is calculated. As was described in the previous sections, the key role is played by the scattering path operator $\tau_{LL'}^{nn}(E)$, which allows to calculate the charge at each SCF iteration and the new potentials that are used to generate the new LSDA Green's function. In practice it turns out that the self-energy converges faster than the charge density. Of course double counting corrections have to be considered explicitly when calculating the total energy. Concerning the self-energy used in the applications presented below the double counting corrections are included when solving the many-body problem (see Ref. [30]).

3.6 Treatment of disordered alloys

Using a local mean-field approximation to treat electron correlations, the corresponding self-energy gets diagonal in the site representation. This allows to use the coherent potential alloy theory (CPA) [19] for the configurational averaging as suggested by Drchal et al. [11]. These authors pointed out that an averaged coherent potential for disordered interacting systems can be constructed using the so-called terminal-point approximation when dealing with disordered alloys, as it was suggested.

Among the electronic structure theories, those based on the multiple scattering formalism are the most suitable to deal with disordered alloys within the CPA. This scheme is considered to be the best theory among the so-called single-site (local) alloy theories that assume complete random disorder and ignore short-range order [20]. Combining the CPA with multiple scattering theory leads to the KKR-CPA scheme, which is applied nowadays extensively for quantitative investigations of the electronic structure and properties of disordered alloys [20, 49]. Within the CPA the configurationally averaged properties of a disordered alloy are represented by an auxiliary ordered CPA-medium, which in turn may be described by a corresponding site-diagonal ($n = m$) scattering path operator $\underline{\tau}^{\text{CPA}}$. The corresponding single-site t -matrix $\underline{t}^{\text{CPA}}$ and multiple scattering path operator $\underline{\tau}^{\text{CPA}}$ are determined by the so called CPA-condition:

$$x_A \underline{\tau}^A + x_B \underline{\tau}^B = \underline{\tau}^{\text{CPA}}. \quad (40)$$

Here a binary system A_xB_{1-x} with relative concentrations $x_A = x$ and $x_B = 1-x$ is considered. The above equation represents the requirement that embedding substitutionally an atom (of type A or B) into the CPA medium should not cause additional scattering as illustrated by Fig. 8. The

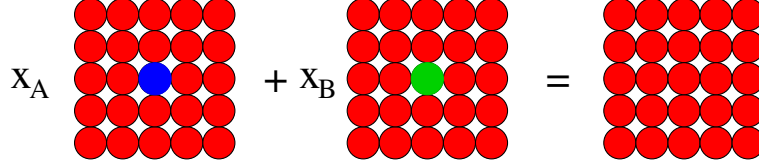


Fig. 8: *The major ideas of the CPA: The configurational average over all configurations of a disordered alloy A_xB_{1-x} is represented by an auxiliary CPA medium. Embedding of an A or B atom should not give rise to additional scattering with respect to the CPA medium.*

scattering properties of an A atom embedded in the CPA medium, are represented by the site-diagonal component-projected scattering path operator $\underline{\mathcal{T}}^A$

$$\underline{\mathcal{T}}^A = \underline{\mathcal{T}}^{\text{CPA}} \left[1 + (\underline{t}_A^{-1} - \underline{t}_{\text{CPA}}^{-1}) \underline{\mathcal{T}}^{\text{CPA}} \right]^{-1}, \quad (41)$$

where \underline{t}_A and $\underline{t}_{\text{CPA}}$ are the single-site matrices of the A component and of the CPA effective medium. A corresponding equation holds also for the B component in the CPA medium. The coupled sets of equations for $\underline{\mathcal{T}}^{\text{CPA}}$ and $\underline{t}^{\text{CPA}}$ have to be solved iteratively within the CPA cycle. It is obvious that the above scheme can straightforwardly be extended to include the many-body correlation effects for disordered alloys. As was pointed above, within the KKR+DMFT approach the local multi-orbital and energy dependent self-energy $\Sigma_{A(B)}$ is directly included in the single-site matrices \underline{t}^A and \underline{t}^B , respectively. Having solved the CPA equations self-consistently, one has to project the CPA Green's function onto the components A and B by using Eqs. (30) and (41). In Eq. (30) the multiple scattering path operator $\tau_{LL'}^\sigma$ has to be replaced by the component-projected scattering path operator $\tau_{LL'}^{A,\sigma}$ of an A-atom in a CPA medium. The components Green's functions $G_{A(B)}$ are used to construct the corresponding bath Green's functions for which the DMFT self-consistency condition is used according to Eq. (6):

$$\mathcal{G}_{A(B)}^{-1}(E) = G_{A(B)}^{-1}(E) + \Sigma_{A(B)}(E). \quad (42)$$

The many-body solver in turn is used to produce the component specific self-energies $\Sigma_{A(B)}$:

$$\Sigma_{A(B)}(E) = \Sigma_{A(B)}(E)[\mathcal{G}_{A(B)}(E)]. \quad (43)$$

As an example for this Fig. 9 shows the corresponding results of an application to the ferromagnetic alloy system fcc- $\text{Fe}_x\text{Ni}_{1-x}$. As one notes the self-energy for the two alloy components are quite different and show a pronounced concentration dependency. For Fe the results of pure bcc-Fe are given in addition. These demonstrate the strong change of the Fe self-energy that occurs when going from the bcc to the fcc phase with a stronger exchange splitting present for the later one.

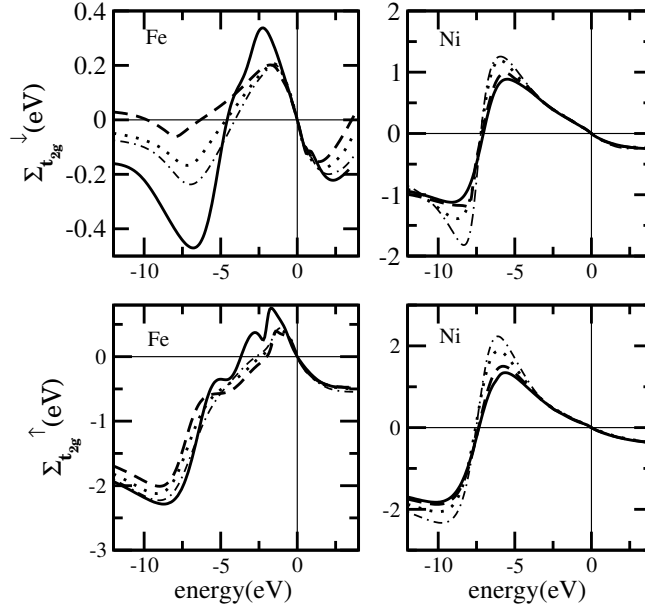


Fig. 9: Left: Concentration dependence of the real part of the spin resolved self-energy for Fe in $\text{Fe}_x\text{Ni}_{1-x}$. Only results for t_{2g} d-orbitals are shown. Right: Same as in the left panel but for Ni. (dashed: $x=0.1$, dotted: $x=0.4$, dash-dotted: $x=0.75$, full: bcc-Fe) [17].

In the alloy system $\text{Fe}_x\text{Ni}_{1-x}$ both components are influenced by correlation effects in a comparable way. For the alloy system $\text{Ni}_x\text{Pd}_{1-x}$, on the other hand, correlation effects should play a minor role for Pd due to the broader width of the d-band. In addition Pd as a pure element is non-magnetic and has a much higher atomic number than Ni. As a consequence one can follow simultaneously the variation of correlation effects, exchange splitting and of spin-orbit splitting in this alloy system when the concentration is varied. Fig. 10 shows a sequence of Bloch spectral functions $A_{\mathbf{B}}(\vec{k}, E)$ for $\text{Ni}_x\text{Pd}_{1-x}$ including the pure elements Ni and Pd. As DMFT-corrections are included only for Ni the Bloch spectral function is smeared out only for Ni, while for Pd a conventional dispersion relation $E_{j\vec{k}}$ emerges. For the alloys additional broadening occurs due to the chemical disorder in the system.

4 Applications

4.1 Ground state properties

The KKR-based implementation of the LSDA+DMFT allows the calculation of a large variety of physical properties of the system under investigation. This permits a direct comparison with experimental data and this way to check the theoretical results. Corresponding studies have been made so far in particular for the magnetic moments in various transition metal systems [43, 17, 40, 50]. Using the relativistic KKR formalism the spin and orbital magnetic moments are obtained as expectation values of the operators $\mu_{\text{B}}\beta\Sigma_z$ and $\mu_{\text{B}}\beta l_z$, resp. (see Eq. (33)). A comparison to experiment for the magnetic moments calculated within the LSDA as well as

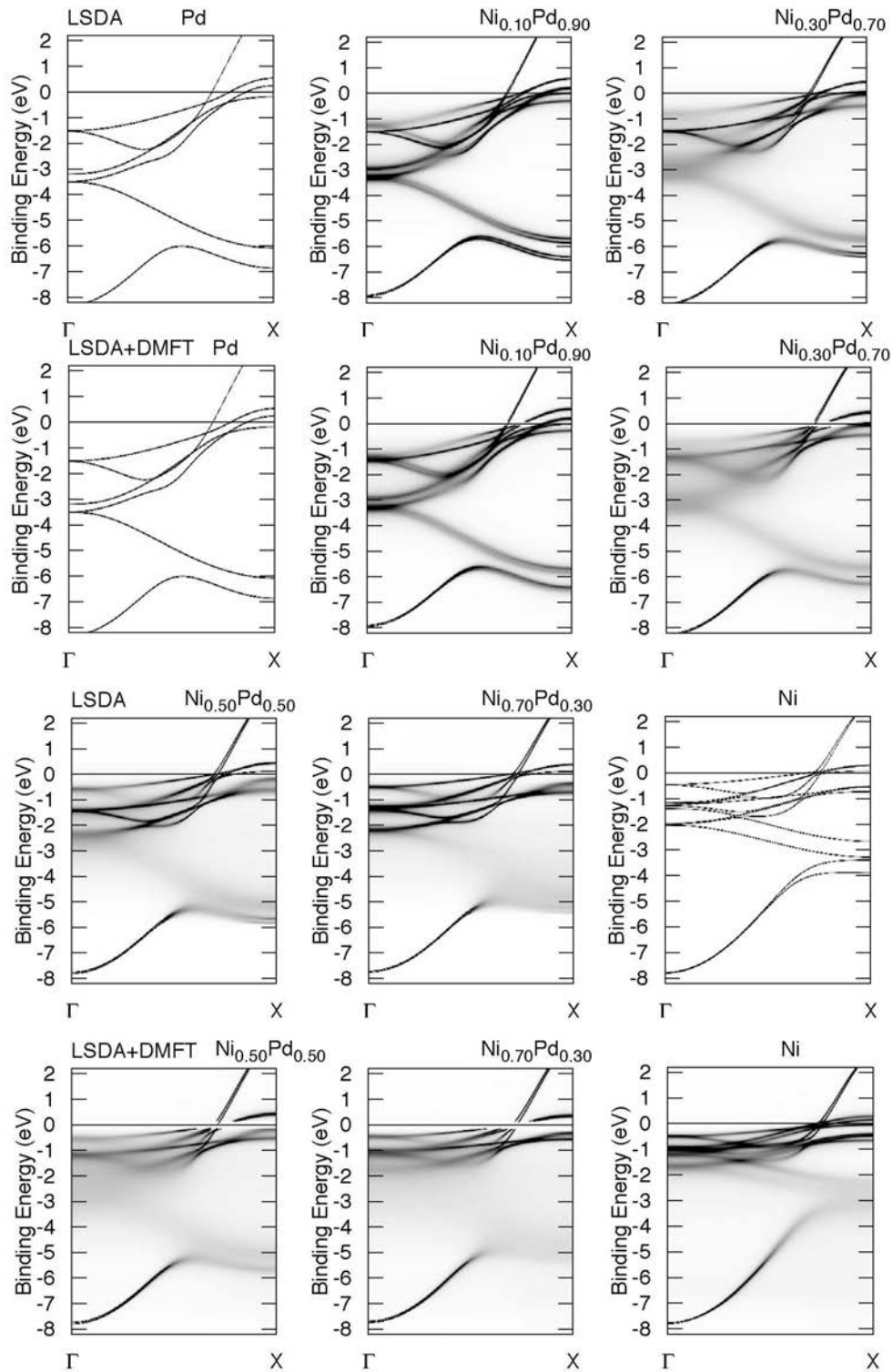


Fig. 10: Spin-polarized Bloch spectral functions for Ni_xPd_{1-x} . Results for LSDA (first and third row) and LSDA+DMFT (second and fourth row) calculations are shown starting from pure Pd (upper panel, left side) to pure Ni (lower panel, right side) [40].

the LSDA+DMFT for bcc Fe, hcp Co and fcc Ni is shown in Fig. 11. The self-energy was parameterized using the values $U = 3$ eV for Co and Ni, and $U = 2$ eV for Fe. As expected, the

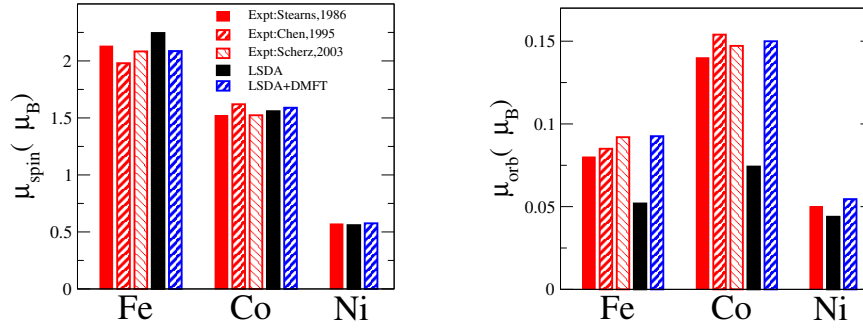


Fig. 11: Spin (left) and orbital (right) magnetic moments in bcc Fe, hcp Co and fcc Ni calculated using LSDA+DMFT (hatched blue bars) compared with plain LSDA calculations (black filled bars) and experimental data (red bars). The corresponding DMFT parameters are $U_{\text{Fe}} = 2$ eV, $U_{\text{Co}} = U_{\text{Ni}} = 3$ eV and $J_{\text{Fe}} = J_{\text{Co}} = J_{\text{Ni}} = 0.9$ eV [43].

LSDA+DMFT approach gives results similar to the orbital polarization (OP) scheme of Brooks [51, 52]: the small orbital splittings imposed by the LSDA+DMFT around the Fermi level have almost no effect on the spin moment, but enhance the orbital moment in an appreciable way.

By construction the dynamical part of the self-energy Σ in the vicinity of the Fermi level behaves like that of a Fermi liquid. Thus it cannot noticeably affect integral quantities as spin and orbital magnetic moments. On the other hand, the applied AMF (around mean field) static double counting which splits the orbitals only slightly at the Fermi level, has no impact on the renormalization of the density of states. As a consequence from Fig. 2, the total DOS curves calculated within LSDA and LSDA+U as well as within LSDA+ Σ (i.e. only the dynamical part of the self energy is used) and LSDA+DMFT are nearly indistinguishable [43]. As the energy shifts of the $(-m, -m)$ and (m, m) matrix elements of the Green's function occur in opposite directions, the total DOS shift for a given spin character appears to be small. As a result, the most affected quantity is the orbital magnetic moment while the change of the spin moment is negligible. At the same time the renormalization of the spectrum is controlled by the dynamical part of the self-energy (see below).

It follows from the various DMFT studies as well as from the DMFT+GW-based calculation [53] that realistic values of U for 3d-TMs are found between 2-3 eV. As it is shown in Fig. 11 this range of U parameters brings both spin and orbital moments into very close agreement with experiment. In the case of Fe the deviation of the orbital moment for U above 2 eV are found to be rather big [43], so that the optimal values of U are confined within 1.5-2 eV. On the other hand, it was already proposed [54] that the local approximation (DMFT) works much better for Ni and Co than for Fe due to relative softness of magnons in the latter case. Recently, the essential non-locality of correlation effects in Fe was also demonstrated experimentally by angle-resolved photo emission [55].

The KKR formalism offers a great flexibility concerning the geometry of the investigated sys-

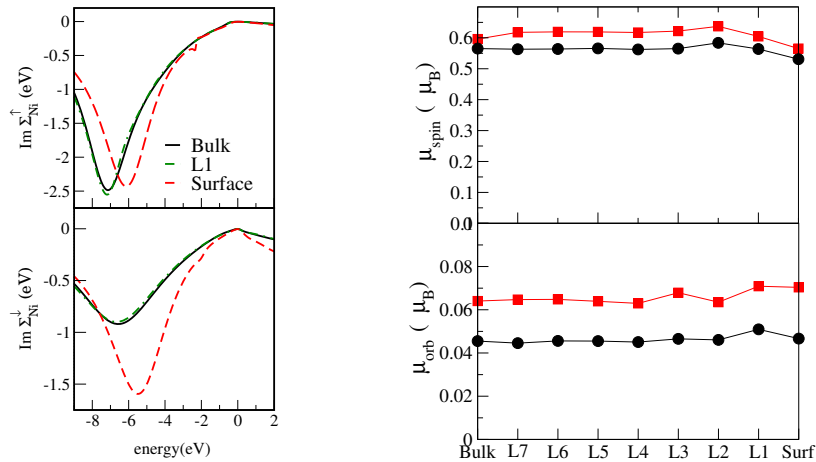


Fig. 12: Left: Spin-dependent self-energy $\Sigma^{\uparrow(\downarrow)}$ for the surface, sub-surface (L1) and bulk-like atomic layers at the (100)-surface of Ni. Right: spin (top) and orbital (bottom) magnetic moments for the individual atomic layers of the (100)-surface of Ni calculated via the LSDA (circles) and LSDA+DMFT (squares) (unpublished).

tem. An example for this is the treatment of surface systems that are usually described in an approximate way by using a film geometry. Within KKR formalism one may consider a number surface near atomic layers on top of a half-infinite bulk-like substrate. As an example Fig. 12 shows some preliminary results for the (100)-surface of Ni for which the 8 top most layers were allowed to relax concerning the charge and potential. As one can see in the left part of the figure the self-energy approaches very rapidly the bulk; already the subsurface layer (L1) has a self-energy very close to that for the bulk. The spin and orbital magnetic moments, however, show an oscillatory behavior very similar to that found within LSDA-calculations.

As described above, a combination of the KKR with the CPA alloy theory allows to deal straight forwardly with disordered alloys. This appealing feature has been exploited so far to study among others the impact of correlations effects on the alloy systems $\text{Fe}_x\text{Ni}_{1-x}$ [17], $\text{Fe}_x\text{Co}_{1-x}$ [43] and $\text{Ni}_x\text{Pd}_{1-x}$ [40]. Corresponding results for the spin and orbital magnetic moments of $\text{Fe}_x\text{Co}_{1-x}$ are shown in Fig. 13. As can be seen from this figure, while the spin magnetic moments for all approaches agree rather well, LSDA+DMFT considerably improves the orbital moments in comparison to plain LSDA calculations in a way similar to the result obtained using the LSDA+OP combined with the CPA [52]. Also in contrast to both the LSDA and LSDA+OP calculations, a better agreement with experimental spin magnetic moments is achieved by LSDA+DMFT within the Fe-rich area of concentrations.

Bulk fcc Ni is a sort of standard test-case for every approach to correlated materials. For this reason it has been chosen for first KKR-based investigations on the influence of correlation effects on the total energy [56]. For this purpose LSDA+DMFT calculations on fcc Ni for various lattice constants starting from $a = 6.2$ a.u. and up to $a = 7.4$ a.u. have been performed. The local DMFT problem was studied for different values of U in the range between 2 and 3 eV, considered acceptable from the results of constrained LSDA calculations [58, 59] and previous

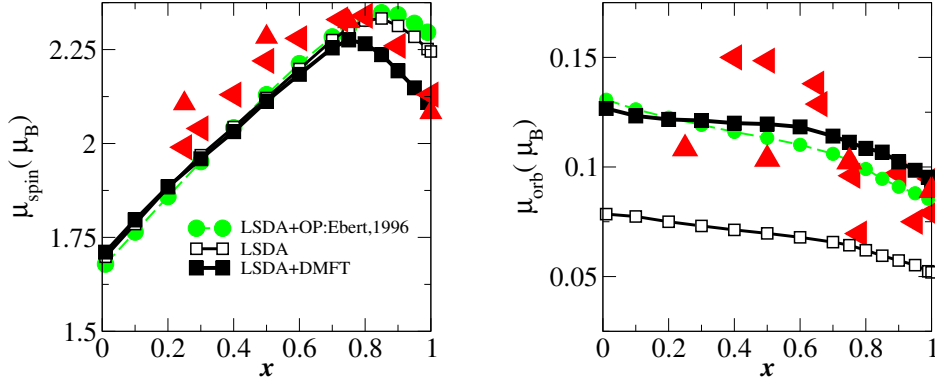
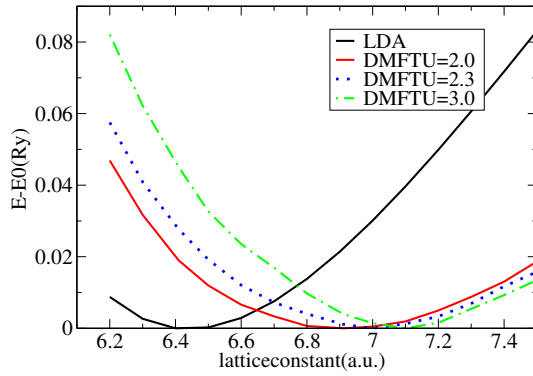


Fig. 13: Spin (left) and orbital (right) total magnetic moments of *bcc* Fe_xCo_{1-x} alloys calculated via LSDA+DMFT (filled squares), compared to plain LSDA (open squares), LSDA+OP calculations [52] (filled circles), and experimental data (red triangles). The corresponding DMFT parameters are $U_{Fe} = 2$ eV, $U_{Co} = 3$ eV and $J_{Fe} = J_{Co} = 0.9$ eV [43].



$U=2\text{eV}$ $J=0.9\text{eV}$	volume (a.u.) ³	bulk mod. (GPa)
LSDA	66.86	280
DMFT (LMTO)	76.20	163
DMFT (KKR)	76.28	171
Expt.	73.52	186

Fig. 14: Left: Energy versus lattice-constant curves for *fcc* Ni in the LSDA and in the LSDA+DMFT scheme. The zero of the energy of each curve is set to its own minimum value E_0 and three chosen values of U are presented ($T = 400$ K). Right: Computed values of the equilibrium atomic volume V_0 and the bulk modulus B of *fcc* Ni for the standard LSDA and for the LSDA+DMFT scheme [57].

LSDA+DMFT simulations. The temperature was set as $T = 400$ K and 2048 Matsubara frequencies were used. As for the DFT part, convergence in the LSDA+DMFT total energy was considered acceptable when the changes for subsequent iterations were smaller than 0.1 meV. On the left-hand side of Fig. 14, one can see the total energy curves as functions of the lattice constant for the KKR implementation. The curves have been shifted with respect to their minima, so it is easier to compare them. As observed in previous calculations [60], in LSDA the equilibrium value of the lattice constant is slightly (3%) underestimated with respect to the experimental one. Looking at the curves for the LSDA+DMFT simulations, one immediately notices that the results are strongly dependent on the value of the Hubbard U . Furthermore the best result seems to be obtained for $U = 2$ eV, i.e. for a value smaller than the widely accepted $U = 3$ eV. On the other hand, the curve for $U = 3$ eV seems to overestimate corre-

lation effects. The explanation of these results is in the perturbative nature of the SPTF solver, which tends to overestimate correlation effects in fcc Ni. This was noticed since the first implementation [30], when comparison between LSDA+DMFT results with the SPTF solver and numerically exact Quantum Monte-Carlo solver showed the best agreement for $U = 2$ eV. Furthermore in the already mentioned calculation of the orbital polarization of Ni, it is shown that SPTF with $U = 3$ eV gives too strong a correction to the orbital moment [43]. The table on the right-hand side of Fig. 14, where the equilibrium atomic volume V_0 and the bulk modulus B are given, allows a more quantitative comparison of implementations of the DMFT using the KKR and LMTO respectively, and with previous LSDA studies of fcc Ni [60]. These values of V_0 and B have been computed with polynomial fitting of the energy versus atomic volume curve around the minimum. In addition also fitting through Birch-Murnaghan equation of state [61] was done, leading to almost identical results and confirming the stability of the data.

As for the total energy curves, the best results are obtained for $U = 2$ eV, and one can see that the inclusion of local correlation effects into the LSDA results corrects both the equilibrium atomic volume and the bulk modulus in the right way. While this fact is interesting on its own, one should notice that to have more precise results from a quantitative point of view, a more strict relation between solver, correlated orbitals and values of U is needed. Naturally it would be interesting to repeat these calculations with the numerically exact quantum Monte-Carlo solver to check if better agreement with the experiment can be obtained. Another interesting property can be deduced from the table on the right-hand side of Fig. 14: while the equilibrium atomic volumes are independent of the full self-consistency, the bulk modulus looks to be more strongly influenced. As expected, this discrepancy is proportional to the strength of U .

4.2 Electron spectroscopy

Photo emission is an experimental tool that allows to probe the electronic structure of a solid in a most detailed way. An appropriate theoretical description can be given on the basis of the one-step model that treats the excitation process, the transfer of the photo electron to the surface as well as its escape to the vacuum in a coherent way [22]. Within this framework the photo current intensity is written as:

$$j_{\vec{k}m_s}^{\vec{q}\lambda}(E + \omega) \propto \int d^3r \int d^3r' \left[\mathcal{T}_R \phi_{\vec{k}m_s}^{\text{LEED}}(\vec{r}, E + \omega) \right]^\dagger X_{\vec{q}\lambda}(\vec{r}) \Im G(\vec{r}, \vec{r}', E) X_{\vec{q}\lambda}^\dagger(\vec{r}') \mathcal{T}_R \phi_{\vec{k}m_s}^{\text{LEED}}(\vec{r}', E + \omega). \quad (44)$$

Here the manifold of initial states is represented in terms of the one-electron Green's function $G(\vec{r}, \vec{r}', E)$. Within a fully relativistic approach, the interaction of the electrons with the radiation field is described by the operator $X_{\vec{q}\lambda}$ that involves the electronic current density operator $\vec{j} = -|e|c\vec{\alpha}$ and the polarization vector $\vec{A}_{\vec{q}\lambda}$ of the radiation with frequency ω . Furthermore, the final state is written as a so-called time-reversed LEED-state that is expressed by a Lippmann-Schwinger equation with the free-electron wave function $\Xi_{m_s} e^{i\vec{k}\vec{r}}$ [47] used as a reference:

$$\phi_{\vec{k}m_s}^{\text{LEED}}(\vec{r}, E) = \Xi_{m_s} e^{i\vec{k}\vec{r}} + \int d^3r' G(\vec{r}, \vec{r}', E) V(\vec{r}') \Xi_{m_s} e^{i\vec{k}\vec{r}'} . \quad (45)$$

Implementation of these expressions using the KKR formalism allows, first of all, a proper description of all geometrical aspects of a photo emission experiment [22]. This includes in particular the surface of the sample as well as the directions of the incoming photo and outgoing electron beams. With a proper relativistic treatment of the transition matrix elements all types of dichroism can be dealt with including the spin polarization of the photo electrons.

Eqs. (44) and (45) allow the calculation of photo electron intensities as measured by a spin and angle resolved photo emission (ARPES) experiment. Averaging over the emission angle allows to discuss the spectra of an angle integrated experiment. The results of a corresponding combined experimental and theoretical study on the pure ferromagnetic metals Fe, Co and Ni in the soft X-ray regime ($\hbar\omega = 600$ eV) are shown in Fig. 15 [45]. The upper panel shows the spin-averaged spectra calculated on the basis of the LSDA and LSDA+DMFT in comparison with experiment. Taking into account the influence of the secondary electrons the theoretical results for the VB-XPS spectra are in fairly good agreement with experiment in the case of Fe and Co. For Ni, on the other hand, the LSDA-based calculations lead to a band-width that is much too large. Furthermore they are not able to reproduce the satellite at about 6 eV binding energy. In case of the LSDA+DMFT calculations, on the other hand, the appreciable real part of the self-energy $\Sigma(E)$ gives rise to a corresponding shrinking of the d-band width of Ni (compare with discussion of the DOS in Fig. 5). This leads to a much better agreement of the theoretical VB-XPS spectrum with experiment, as can be seen in Fig. 15. In addition, use of the LSDA+DMFT scheme leads to a pronounced increase of the intensity in the regime of the 6 eV satellite. The bottom row of Fig. 15 gives the spin difference of the photo-current ΔI^+ ,

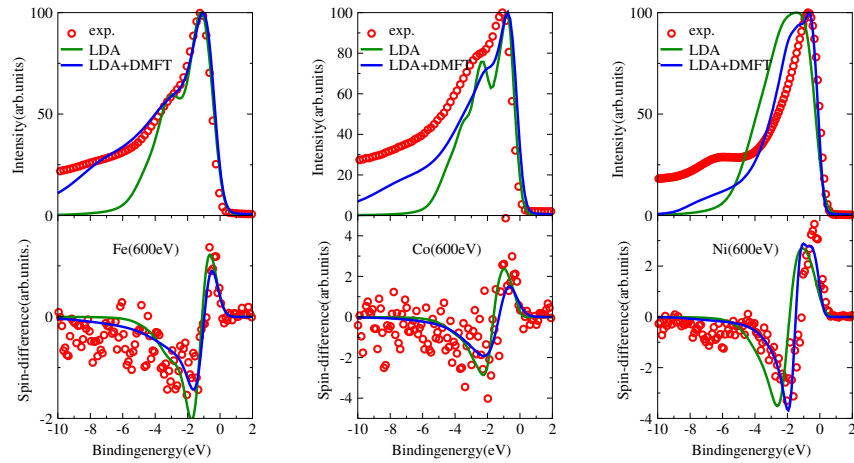


Fig. 15: Top: spin and angle-integrated VB-XPS spectrum of ferromagnetic Fe (left), Co (middle), and Ni (right) for a photon energy of 600 eV. Bottom: spin difference $\Delta I = I_{\uparrow}^+ - I_{\downarrow}^+$ of the photo current for excitation with left circularly polarized radiation. Theory: solid line; experiment: dashed line. The same scale has been used for the intensity and corresponding spin-difference plots [45].

i.e. the difference of the currents of photo-electrons with spin-up and spin-down with respect to the surface normal, for an excitation with left circularly polarized radiation. Because the

polarization analysis of the photo-current is done with respect to an axis that is perpendicular to the spontaneous magnetization \vec{m} (oriented parallel to the surface), ΔI^+ cannot be caused by the exchange splitting of the ground state. In fact ΔI^+ is caused by the Fano-effect. This term denotes the fact that the spin-orbit coupling together with the transition selection rules gives in general rise to a spin-polarized photo electron beam - even in case of non-magnetic solids.

As for the total intensity, the theoretical spin difference ΔI^+ shown in the bottom row of Fig. 15 is found in rather good agreement with experiment in particular for Fe and Co. The sequence for the maximum (minimum) of ΔI^+ of Fe, Co and Ni is found to be 1.3, 2.2 and 2.6 (-1.9, -2.7 and -3.5). Although there are several electronic and structural properties that determine these data, they nevertheless correlate reasonably well with the strength of the spin-orbit coupling parameters of the d-states (66, 85 and 107 meV, respectively) [62] to identify once more the spin-orbit coupling as the source for the observed spin-polarization. As for the standard VB-XPS spectra inclusion of the self-energy $\Sigma(E)$ leads to a substantial improvement for the agreement of the theoretical ΔI^+ spectrum with experiment. As one can see in Fig. 15, the shrinking of the band width is also reflected by the ΔI^+ curves, while their amplitude and shape is only slightly changed.

Performing photo emission experiments in the angle-resolved mode (ARPES) obviously supplies much more detailed information on the electronic structure than angle-integrated experiments. If no specific surface-related features show up in the spectra the observed peaks in an ARPES spectrum may be interpreted qualitatively to reflect the dispersion relation $E_{j\vec{k}}$ via vertical transitions ($\Delta\vec{k} = 0$) to free-electron like final states. Fig. 16 shows corresponding experimental and theoretical ARPES spectra for the (110) surface of Ni with the initial state \vec{k} vector along $\overline{\Gamma Y}$ and different angles of emission. The dotted lines represent the experimental data, whereas the solid lines denote the one-electron approach to the measured spectral function. Obviously, the LSDA-based (top row) calculation completely fails. The energetic positions of the theoretical peaks deviate strongly from the measured ones. Furthermore, the complicated intensity distributions that appear for higher angles of emission could not be reproduced by the LSDA method at all. In contrast, the non-selfconsistent quasi particle calculation based on the three-body scattering formalism of Manghi et al. [63] provides a significant improvement when compared to the measured spectra. For the complete variety of emission angles the energetic peak positions coincide with the experiment within about 0.1 eV.

Only the overall shape of the measured spectral intensities deviate from the calculations because of the neglect of multiple scattering and surface-related effects. In the experiment the different peaks seem to be more broadened and the spectral weight especially for nearly normal emission is shifted by about 0.1 eV to higher binding energies. In addition, it seems that for very high emission angles like 60° an even more complicated peak structure is hidden in the experimental resolution. KKR calculations allowed to go far beyond previous theoretical studies by combining the self-consistent LSDA DMFT method with the one-step based calculation of the corresponding spectral function. The resulting intensity distributions are shown in the lower row of Fig. 16. A first inspection reveals very satisfying quantitative agreement between

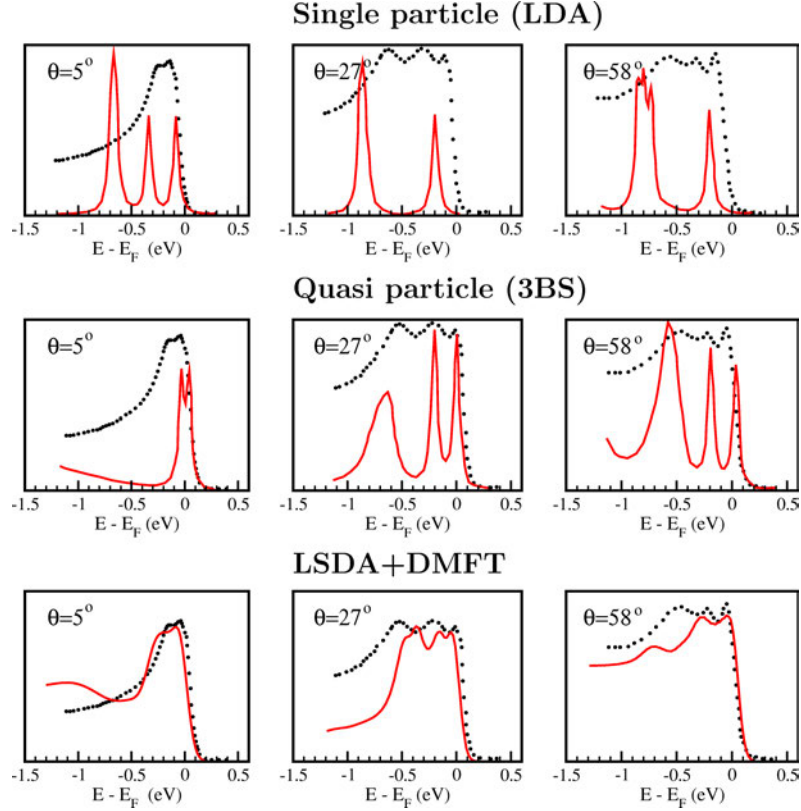


Fig. 16: Spin-integrated ARUPS spectra from Ni(110) along $\overline{\Gamma Y}$ for three different angles of emission. Upper row: comparison between LSDA-based calculation and experiment [63], middle row: comparison between experiment and non-self-consistent quasi particle calculations neglecting matrix element and surface effects [63], lower row: spin-integrated LSDA+DMFT spectra including photo emission matrix elements (this work). Theory: solid red line, experiment: black dots [44].

experiment and theory for all emission angles. For the emission angle 5° the spin-integrated spectrum exhibits a pronounced double-peak structure with binding energies of 0.1 eV and 0.3 eV. The second peak is slightly reduced in intensity which is also in accordance with the experimental findings. Furthermore, the width of the spectral distribution is quantitatively reproduced. The calculated binding energies can be ascribed to the real part of the self-energy that corrects the peak positions due to dynamical renormalization procedure of the quasi particles which is missing in a typical LSDA-based calculation. The relative intensities and the widths of the different peaks, on the other hand, must be attributed to the matrix-element effects which enter the calculations from the very beginning via the one-step model of photo emission. As it has been found for Ni(001) the double-peak structure originates from excitation of the spin-split d bands in combination with a significant amount of surface-state emission [11]. The two spectra calculated for high angles of emission show the more broadened spectral distributions observable from the experimental data. An explanation can be given in terms of matrix-element effects, due to the dominating dipole selection rules. The spin-resolved spectra reveal a variety of d-band excitations in both spin channels, which in consequence lead to the complicated shape of the

spectral distributions hardly to be interpreted in the spin-integrated mode.

Spin-resolved ARPES experiments have been made recently for the elemental ferromagnets Fe, Co and Ni [55, 64]. Fig. 17 displays a comparison between spin-resolved ARPES data and theoretical LSDA+DMFT calculations of Fe(110) along the $\overline{\Gamma\text{N}}$ direction of the bulk Brillouin zone (BZ) for p- and s-polarized photons together with LSDA+DMFT calculations. The k

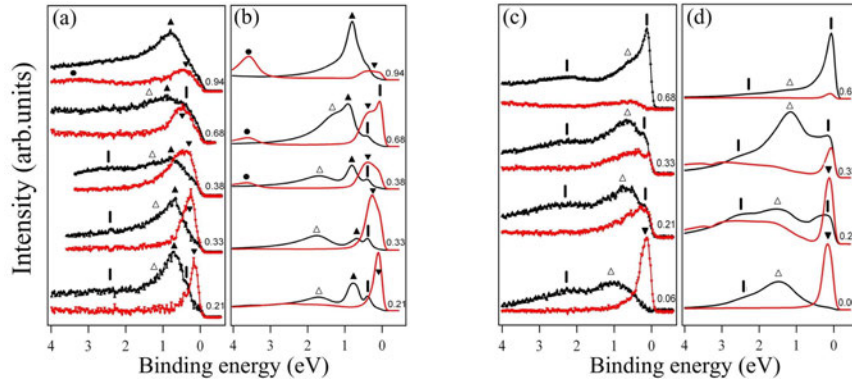


Fig. 17: Spin-resolved ARPES spectra of Fe(110) in normal emission along $\overline{\Gamma\text{N}}$. The curves are labeled by k in units of $\overline{\Gamma\text{N}}=1.55 \text{ \AA}^{-1}$. (a), (c) Experiment [upwards (black) triangles: majority states, downwards (red) triangles: minority states]. (b), (d) LSDA+DMFT theory [dark (black) and light (red) lines for majority and minority electrons, respectively]. (a), (b) For p- and (c), (d) for s polarization [55].

values were calculated from the used photon energies ranging from 25 eV to 100 eV, using an inner potential $V=14.5$ eV.

Near the Γ point ($k \sim 0.06 \overline{\Gamma\text{N}}$), the intense peak close to the Fermi level corresponds to a $\Sigma_{1,3}^\downarrow$ minority surface resonance. Experimentally, its Σ_3^\downarrow bulk component crosses the Fermi level at $k \sim 0.33 \overline{\Gamma\text{N}}$, leading to a reversal of the measured spin-polarization and to a strong reduction of the intensity at $k = 0.68 \overline{\Gamma\text{N}}$ in the minority channel, in agreement with the theoretical results (Fig. 17 (b) and (d)). The peak at the binding energy $\text{BE} \sim 0.7$ eV, visible mainly for p-polarization in a large range of wave vectors between Γ and N can be assigned to almost degenerate $\Sigma_{1,4}^\uparrow$ bulk-like majority states (Figs. 17 (a) and (b)). For s-polarization (Fig. 17 (c) and (d)), a Σ_3^\uparrow feature at $\text{BE} \sim 1.1$ eV dominates the spectrum at the Γ point. For p-polarization its degenerate Σ_1^\uparrow states form a shoulder around the same BE. The broad feature around 2.2 eV, visible at various k points, but not at the N point, is related to a majority $\Sigma_{1,3}^\uparrow$ surface state (see below). Around the N-point ($0.76 \leq k \leq 1.0$) and at $\text{BE} \geq 3$ eV (Figs. 17 (a)) one observes a Σ_1^\downarrow band having strong sp-character. The pronounced difference between its theoretical and experimental intensity distributions can be attributed to the fact that in the calculations only local Coulomb repulsion between d-electrons is considered, without additional lifetime effects for the sp-bands. Finally, one notices that the background intensity of the spectrum at $k=0.66 \overline{\Gamma\text{N}}$, corresponding to a photon energy of 55 eV, is strongly increasing by the appearance of the Fe 3p resonance. Comparing the experimental results from spin-integrated and spin-resolved ARPES measurements with LSDA+DMFT results, one obtains at low BE good agreement for many of

the peak positions. This is also demonstrated in Fig. 18 (a) and (b) where the experimental peak positions are compared with the LSDA+DMFT spectral function. Similar calculations based on the LSDA+3BS scheme are compared with the experimental data in Fig. 17(a) and (c). Since the theoretical calculations do not show big differences, also the LSDA+3BS spectral function agrees well at low BE with the experimental peak positions. On the other hand, quantitative

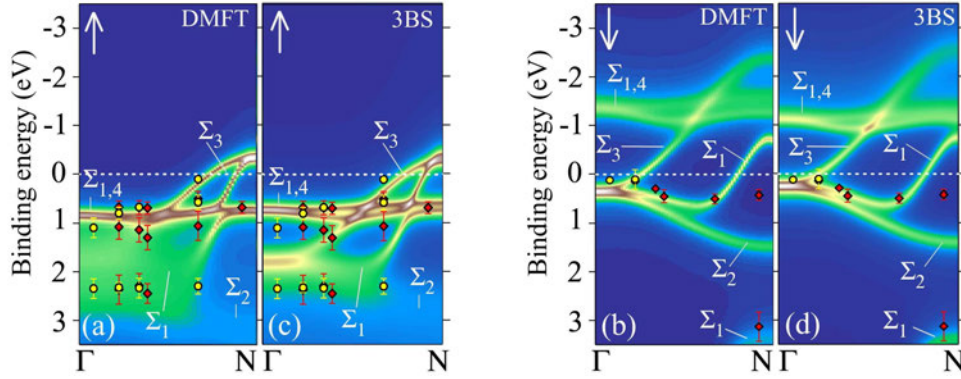


Fig. 18: Spectral functions of Fe(110) and photo emission peak positions obtained from the spin-resolved measurements for different polarizations (Diamonds for horizontal and circles for vertical polarization). Results obtained by LSDA+DMFT ((a), (b)) and by LSDA+3BS ((c), (d)) methods for majority and minority electronic states, respectively [55].

agreement cannot be achieved for higher BE. In particular, the calculated spectral weight near Γ for the $\Sigma_{1,3}^\uparrow$ bands is in between the experimental features at 1.2 eV and 2.2 eV. Assuming negligible correlation effects would move the calculated feature to the LSDA value at BE=2.2 eV. Thus the experimental peak at 2.2 eV could be assigned to the bulk $\Sigma_{1,3}^\uparrow$ bands. However, a complete neglect of correlation effects in Fe would make the overall comparison between theory and experiment much worse. Thus the experimental peak at BE=2.2 eV is interpreted as a $\Sigma_{1,3}^\uparrow$ surface state in agreement with previous experimental and theoretical studies [65]. The theoretical results confirm this view since one clearly observes how changes in the surface barrier potential induce additional shifts in its BE position. Thus, from the data shown in Fig. 18 one can conclude that correlation effects in the calculations using $U=1.5$ eV are underestimated and that a stronger band narrowing is needed to achieve agreement between theory and experiment.

Other investigations on spectroscopic properties using the implementation of the LSDA+DMFT via the KKR method were dealing so far with the magneto-optical Kerr effect, the magnetic X-ray dichroism in X-ray absorption and the magnetic Compton effect. As for the photo emission considered here, it turned out that treatment of correlation effects via the DMFT substantially improves agreement with experiment compared to plain LSDA calculations.

5 Summary

The implementation of the LSDA+DMFT on the basis of the KKR method has been described in some detail. The appealing feature of this approach is that the KKR delivers the one-electron

Green's function directly. It therefore allows to combine the treatment of correlations via the DMFT with calculation of a great variety of physical properties for, in principle, any type of system. As was demonstrated by results for magnetic moments and photo emission spectra of various transition metal systems, this allows in particular a direct comparison with experiment.

Acknowledgment

This work was supported by the Deutsche Forschungsgemeinschaft through FOR 1346, EB-154/18, EB-154/23 and MI-1327/1 and by the BMBF (Project 05KS10WMA).

References

- [1] A.I. Lichtenstein, M.I. Katsnelson, and G. Kotliar, in *Electron Correlations and Materials Properties II*, edited by A. Gonis, N. Kioussis, and M. Ciftan (Kluwer/Plenum, Berlin, 2002), p. 428
- [2] K. Held *et al.*, in *Quantum Simulations of Complex Many-Body Systems: From Theory to Algorithms*, NIC Series, edited by J. Grotendorst, D. Marx, and A. Muramatsu (NIC, Jülich, 2002), Vol. 10, p. 17
- [3] K. Held, *Adv. Phys.* **56**, 829 (2007)
- [4] G. Kotliar *et al.*, *Rev. Mod. Phys.* **78**, 865 (2006)
- [5] V. I. Anisimov *et al.*, *J. Phys.: Cond. Mat.* **9**, 7359 (1997)
- [6] A. I. Lichtenstein and M. I. Katsnelson, *Phys. Rev. B* **57**, 6884 (1998)
- [7] M. Katsnelson and A. Lichtenstein, *J. Phys.: Cond. Mat.* **11**, 1037 (1999)
- [8] S.Y. Savrasov, G. Kotliar, and E. Abrahams, *Nature* **410**, 793 (2001)
- [9] S.Y. Savrasov and G. Kotliar, *Phys. Rev. B* **69**, 245101 (2004)
- [10] L. Chioncel, M.I. Katsnelson, R.A. de Groot, and A. I. Lichtenstein, *Phys. Rev. B* **68**, 144425 (2003)
- [11] V. Drchal, V. Janiš, and J. Kudrnovský, *Phys. Rev. B* **60**, 15664 (1999)
- [12] L. Chioncel *et al.*, *Phys. Rev. B* **67**, 235106 (2003)
- [13] O.K. Andersen and T. Saha-Dasgupta, *Phys. Rev. B* **62**, R16219 (2000)
- [14] L. Vitos, H.L. Skriver, B. Johansson, and J. Kollar, *Comp. Mater. Science* **18**, 24 (2000)
- [15] A. Schindlmayr, P. García-González, and R. W. Godby, *Phys. Rev. B* **64**, 235106 (2001)
- [16] L. Vitos, *Phys. Rev. B* **64**, 014107 (2001)
- [17] J. Minár *et al.*, *Phys. Rev. B* **72**, 045125 (2005)
- [18] H. Ebert, D. Ködderitzsch, and J. Minár, *Rep. Prog. Phys.* in the press (2011)
- [19] P. Soven, *Phys. Rev.* **156**, 809 (1967)
- [20] J.S. Faulkner, *Progress in Materials Science* **27**, 1 (1982)
- [21] A. Georges, G. Kotliar, W. Krauth, and M.J. Rozenberg, *Rev. Mod. Phys.* **68**, 13 (1996)
- [22] J. Braun, *Rep. Prog. Phys.* **59**, 1267 (1996)

-
- [23] H. Ebert, Rep. Prog. Phys. **59**, 1665 (1996)
- [24] D. Sébilleau *et al.*, J. Phys.: Cond. Mat. **18**, R175 (2006)
- [25] J. Koringa, Physica **13**, 392 (1947)
- [26] W. Kohn and N. Rostoker, Phys. Rev. **94**, 1111 (1954)
- [27] V.I. Anisimov, J. Zaanen, and O.K. Andersen, Phys. Rev. B **44**, 943 (1991)
- [28] V.I. Anisimov, F. Aryasetiawan, and A.I. Lichtenstein, J. Phys.: Cond. Mat. **9**, 767 (1997)
- [29] L.V. Pourovskii, M.I. Katsnelson, and A.I. Lichtenstein, Phys. Rev. B **72**, 115106 (2005)
- [30] M.I. Katsnelson and A.I. Lichtenstein, European Physics Journal B **30**, 9 (2002)
- [31] R. Harris, J. Phys. C: Solid State Phys. **3**, 172 (1970)
- [32] R. Zeller, J. Phys. C: Solid State Phys. **20**, 2347 (1987)
- [33] E. Tamura, Phys. Rev. B **45**, 3271 (1992)
- [34] H. Ebert and B.L. Györffy, J. Phys. F: Met. Phys. **18**, 451 (1988)
- [35] J.S. Faulkner and G.M. Stocks, Phys. Rev. B **21**, 3222 (1980)
- [36] A. Gonis and W.H. Butler, *Multiple scattering in solids, Graduate Texts in Contemporary Physics* (Springer, Berlin, 1999)
- [37] B.L. Györffy and M.J. Stott, in *Band Structure Spectroscopy of Metals and Alloys*, edited by D.J. Fabian and L.M. Watson (Academic Press, New York, 1973), p. 385
- [38] J. Zabloudil, R. Hammerling, L. Szunyogh, and P. Weinberger, in *Electron Scattering in Solid Matter*, Vol. 147 of *A Theoretical and Computational Treatise of Springer Series in Solid-state Sciences* (Springer, Berlin, 2005)
- [39] J.S. Faulkner, J. Phys. C: Solid State Phys. **10**, 4661 (1977)
- [40] J. Braun *et al.*, Phys. Rev. B **82**, 024411 (2010)
- [41] X. Dai *et al.*, Science **300**, 953 (2003)
- [42] L.V. Pourovskii, M.I. Katsnelson, and A.I. Lichtenstein, Phys. Rev. B **73**, 60506 (2006)
- [43] S. Chadov *et al.*, Europhys. Lett. **82**, 37001 (2008)
- [44] J. Braun *et al.*, Phys. Rev. Lett. **97**, 227601 (2006)
- [45] J. Minár *et al.*, Phys. Rev. Lett. **95**, 166401 (2005)

-
- [46] A.H. MacDonald and S.H. Vosko, *J. Phys. C: Solid State Phys.* **12**, 2977 (1979)
- [47] M.E. Rose, *Relativistic Electron Theory* (Wiley, New York, 1961)
- [48] H. Ebert, in *Electronic Structure and Physical Properties of Solids*, Vol. 535 of *Lecture Notes in Physics*, edited by H. Dreyssé (Springer, Berlin, 2000), p. 191
- [49] H. Ebert and H. Akai, *Mat. Res. Soc. Symp. Proc.* **253**, 329 (1992)
- [50] S. Chadov *et al.*, *J. Phys. D: Appl. Phys.* **42**, 084002 (2009)
- [51] M.S.S. Brooks, *Physica B* **130**, 6 (1985)
- [52] H. Ebert and M. Battochetti, *Solid State Commun.* **98**, 785 (1996)
- [53] S. Biermann, F. Aryasetiawan, and A. Georges, *Phys. Rev. Lett.* **90**, 086402 (2003)
- [54] A.I. Lichtenstein, M.I. Katsnelson, and G. Kotliar, *Phys. Rev. Lett.* **87**, 067205 (2001)
- [55] J. Sánchez-Barriga *et al.*, *Phys. Rev. Lett.* **103**, 267203 (2009)
- [56] I. Di Marco *et al.*, *Eur. Phys. J. B* **72**, 473 (2009)
- [57] I. Di Marco *et al.*, *Phys. Rev. B* **79**, 115111 (2009)
- [58] A.M. Oles and G. Stollhoff, *Phys. Rev. B* **29**, 314 (1984)
- [59] T. Bandyopadhyay and D.D. Sarma, *Phys. Rev. B* **39**, 3517 (1989)
- [60] M. Černý *et al.*, *Phys. Rev. B* **67**, 035116 (2003)
- [61] F.D. Murnaghan, *Proc. Natl. Acad. Sci. USA* **30**, 244 (1944)
- [62] V. Popescu, H. Ebert, B. Nonas, and P.H. Dederichs, *Phys. Rev. B* **64**, 184407 (2001)
- [63] F. Manghi *et al.*, *Phys. Rev. B* **59**, R10409 (1999)
- [64] J. Sánchez-Barriga *et al.*, *Phys. Rev. B* **82**, 104414 (2010)
- [65] H.J. Kim, E. Vescovo, S. Heinze, and S. Blügel, *Surf. Sci.* **478**, 193 (2001)